5th Joint International Symposium on Deformation Monitoring (JISDM), 20-22 June 2022, Valencia, Spain
DOI: http://doi.org/10.4995/JISDM2022.2022.13632

2D strain rate and ground deformation modelling from continuous and survey mode GNSS data in El Hierro, Canary Islands

Jose Arnoso[1, 2], Umberto Riccardi[2, 3], Umberto Tammaro[4], Maite Benavent[2, 5], Fuensanta G. Montesinos[2, 5], Emilio Vélez[1, 2]

[1] Instituto de Geociencias (CSIC-UCM). C/ Doctor Severo Ochoa 7, 28040 Madrid, Spain, (jose.arnoso@csic.es; emilio.velez@csic.es)
[2] Research Group 'Geodesia', Universidad Complutense de Madrid, Spain
[3] Dipartimento di Scienze della Terra, dell'Ambiente e delle Risorse (DiSTAR), University "Federico II" of Naples, Italy, (umbricca@unina.it)
[4] Istituto Nazionale di Geofisica e Vulcanologia Sezione, "Osservatorio Vesuviano", Naples, Italy, (umberto.tammaro@ingv.it)
[5] Facultad de Matemáticas, Universidad Complutense de Madrid. Plaza de Ciencias 3, 28040 Madrid, Spain, (mbena@ucm.es; fuensant@ucm.es)

Key words: *GNSS; kinematics and ground deformation; Canary Islands*

ABSTRACT

We present a study of the deformation pattern in El Hierro Island through the analysis of GNSS data from surveys carried out between 2015 and 2019 as well as continuous data. The last eruption in El Hierro occurred under the sea on the south rift, lasted from October 2011 to March 2012, and it was preceded by intense seismic activity and nearly 5 cm ground inflation. After this eruptive cycle, further magmatic intrusions were detected, from June 2012 to March 2014, associated to intense seismic swarms and inflation (about 22 cm of uplift). Nevertheless, these magmatic intrusions did not culminate in any eruption. Following these post-eruptive episodes, the seismic activity became less intense. Thus, for the period of this study, about 500 earthquakes with magnitude ranging from m_{bLG} 2 to m_{bLG} 3.9 were recorded, the ground deformation measured is of lower magnitude, still remaining a slight uplift trend in the GNSS stations up to 2017 and followed by a slight subsidence of about 1.5 cm between 2017-2019. Our purpose is to explain the ground displacements measured and the earthquake occurrence in terms of geodynamics and seismotectonic activity along the island, for the period 2015-2019. Firstly, we retrieved the geodetic velocities from the GNSS daily solutions. Secondly, we computed the 2D infinitesimal strain rates from the velocities through a triangular segmentation approach to map the deformation pattern along the respective GNSS surveys.

I. INTRODUCTION

Over the last decade, GNSS has seen enormous advances in the precision and accuracy of measurements. Time series analysis has become a widely used tool for detecting and interpreting very small and slow amplitude displacements of the Earth's surface with sub-centimetre accuracy induced by multiple geodynamic phenomena. Quantifying both in space and time the crustal deformation cycles related to volcanic and tectonic processes are currently the major challenges in tectonic geodesy. Today, continuous GNSS observations collected on permanent networks shed light on crustal movement and deformation processes at high temporal resolution. However, tackling challenging studies such as monitoring volcanoes and detecting pre-eruptive magmatic processes (*e.g.* Segall, 2010; Arnoso *et al.*, 2020) requires the reconstruction of a reliable image of the deformation field. In this case, it is necessary to bridge the spatial resolution gap through the integration of continuous and repeated GNSS observations. In any case, either continuous or precise repeated positioning measurements provide only displacement information for a finite number of points. Therefore, in order to derive local and regional deformation models, it is necessary to apply an interpolation-oriented analysis method to obtain a continuous field. GNSS-derived strain rates have countless applications in studies aimed at comparing stress fields and rates to explain earthquake occurrence or volcano deformation (Tammaro *et al.*, 2013). Currently, there are two possible approaches to estimate strains from GNSS observations. A gridded approach, called least-squares collocation (LSC), which consists of inverting a uniform velocity field to the strain rate field or calculating strain rates in triangular or more complex segments. A very detailed description of the pros and cons of the different methods of strain retrieval can be found in (Wu *et al.*, 2011). Several papers have dealt with the study of geodynamics, tectonic and/or volcanic processes on the Canary Islands using GNSS data and different geodetic techniques, some focused on a specific island (*e.g.*

Berrocoso *et al*., 2010; García *et al*., 2014; Riccardi *et al*., 2018) others on the whole archipelago (Geyer *et al*., 2016; Arnoso *et al*., 2020).

Compiling a regional seismic catalogue and analysing long time series of permanent GPS from a regional network, López *et al*. (2017) detected the first signs of geodynamic activity preceding the El Hierro eruption and subsequent episodes of magma intrusion. Later, the occurrence of six post-eruptive magmatic intrusions during 2012-2014 was studied by Domínguez-Cerdeña *et al*. (2018), and the relation between seismicity and deformation for the period 2011-2014 was recently examined by Pérez-Plaza *et al*. (2021).

Here, we present a study of the deformation pattern in El Hierro Island through the analysis of GNSS data from surveys carried out between 2015 and 2019 as well as continuous data. Our purpose is to explain the ground displacements measured and the earthquake occurrence in terms of geodynamics and seismotectonic activity along the island, for the period 2015-2019. Firstly, we retrieved the GNSS velocities from the daily solutions. Secondly, we computed the 2D infinitesimal strain rates from the velocities through a triangular segmentation approach to map the deformation pattern along the respective GNSS surveys. Our results suggest that magma movement and/or accumulation within the lower crust beneath El Hierro plays an important role in its volcanic evolution in terms of tectonic stresses.

II. Geological Setting

El Hierro Island is the youngest of the Canary Islands archipelago, and corresponds to a volcanic shield structure that includes three rift zones and superimposed volcanoes. The island rises from 4000 m below sea level to a maximum altitude of 1501 m above sea level. The rift zones associated with the typical instability of the volcanic islands, especially in its stage of growth and shield formation due to gravitational tensions, dike injections, magmatic intrusions, etc., they progressively tend to increase the possibility of giant landslides. Presently, there are three collapse scars which appear as steep cliffs or formation of arc-shaped bays, which configure a typical three-armed star morphology in the island's edifice (Figure 1). The emerged parts of the island's rifts are defined by topographic ridges, lying at 120°, corresponding to aligned dike complexes with clusters of cinder cones (Cantagrel *et al*., 1999; Carracedo *et al*., 2001). The ridges concentrate the Holocene volcanism, the most recent being the southern ridge. The 2011-2012 submarine eruption was the last observed in more than 500 years of historical records, and lasted for 5 months. The eruption occurred on a north-south fissure in the southern part of the rift, about 1.8 km from the coast, and built a new 220 m high underwater volcanic edifice (Martí *et al*., 2013; López *et al*., 2017). The eruption started on October 10th and was preceded by 3 months of intense seismic activity, ground deformation (a maximum uplift of about 5 cm in the central El Hierro) and gas emissions. The post-eruptive phase (March 2012 to July 2014) was attached to 6 seismic swarms corresponding to magmatic intrusive events, which took place in different areas and were accompanied by rapid island uplift (2 cm/day) that revealed faster inflation processes than in the eruptive phase (Domínguez-Cerdeña *et al*., 2018). Analysis of seismic and geodetic data suggested that the volume of magma emplaced was also bigger than during the eruptive phase (Klügel *et al*., 2015).

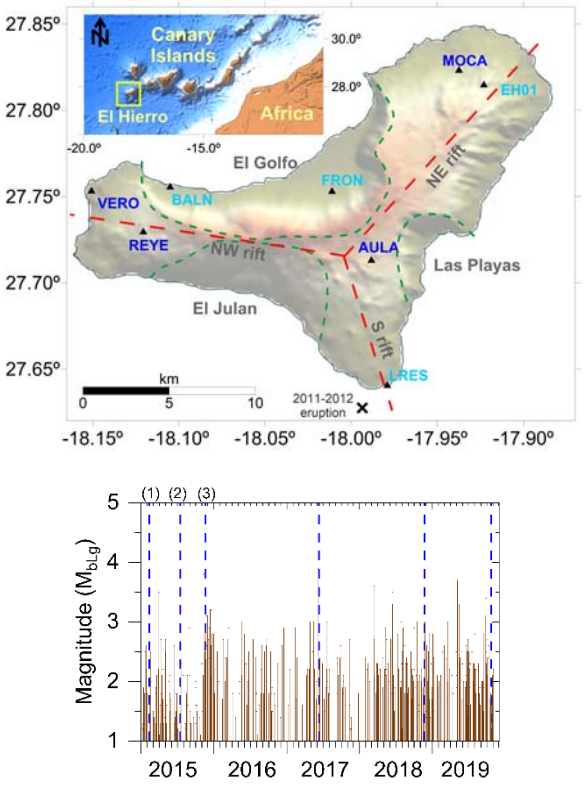

Figure 1. (Up) Relief map of El Hierro (Canary Islands) showing the triple-armed volcanic rift system (dashed red lines), as well as the embayments (green dashed lines) of El Golfo, El Julan, and Las Playas. Black triangles show the location of GNSS sites (blue colour indicate the survey sites and light blue the permanent sites). (Down) Seismicity recorded in El Hierro between 2015 – 2019. Dashed blue lines mark the time of the episodic GNSS surveys used in this study; (1), (2), (3) denote the respective surveys performed during 2015.

III. GNSS Surveys and Data Processing

El Hierro GNSS survey network consists of 8 observing sites, 4 non-permanent and 4 in continuous operating mode (Figure 1). Episodic surveys were made at the sites REYE, VERO, MOCA and AULA in 2015 (3 surveys), 2017, 2018 and 2019 using observation periods ranging from a minimum of 48 hours to a maximum of 96 hours. Additionally, we used data from the permanent GNSS site FRON during all the episodic surveys, and the permanent sites LRES, EH01 for strain calculations in the period from 2018 to 2021. The most recent GNSS

site, BALN, was included in the calculations covering the years 2019 to 2021. The stations EH01 and LRES belong to Spanish Geographical Institute (IGN), whereas FRON belong to the Cartographic Service (GRAFCAN) of the Government of Canary Islands. The station BALN is managed from the Spanish National research Council (CSIC) and the University Complutense of Madrid (UCM). Table 1 lists the geographic coordinates of the 8 observing sites.

Table 1. Example table Location and owner of the GNSS sites in El Hierro used in this study

Site	Long [°]	Lat [°]	h [m]	Owner
BALN	-18.105	27.756	55.5	CSIC-UCM
EH01	-17.923	27.815	800.9	IGN
FRON	-18.011	27.753	308.5	GRAFCAN
LRES	-17.979	27.641	51.1	IGN
MOCA	-17.937	27.823	499.5	CSIC-UCM
REYE	-18.121	27.730	768.1	CSIC-UCM
VERO	-18.151	27.754	78.6	CSIC-UCM
AULA	-17.988	27.714	984.7	CSIC-UCM

All non-permanent sites are managed by the Research Group Geodesy (UCM). The location of the sites has been selected so that they are easily accessible, satisfying suitable geometrical conditions and having homogeneous distance between sites, good satellite visibility and trying to avoid electromagnetic interferences.

We used the Canadian Spatial Reference System Precise Point Positioning (CSRS-PPP) online web service of the Natural Resources of Canada to provide the daily solutions. The service provides Precise Point Absolute Positioning (PPP) for data prior to 2018, and PPP with reliable integer ambiguity resolution for GPS (PPP-AR) from 2018 in advance (Banville, 2020). Both methods allow estimating the station coordinates for the specific epoch using accurate satellite orbit and clock information from the International GPS Service, from the absolute calibration models of the IGS antenna phase-center and from the elimination of systematic errors through the accurate modelling of various error sources, such as ionospheric and tropospheric delays, Earth tide and ocean tide loading, the latter correction uses the GOT4.10 model (Ray, 2013; 1999). For the case of PPP processing, time (P-code modulated on L1 and L2 carrier waves) and phase shift (of L1 and L2 waves) measurements are considered as observables, modeled by forming double differences of a linear free ionosphere combination. Additionally, PPP-AR processing transforms ambiguous carrier-phase observations into precise ranges using a backward run process (Tenuissen and Montenbruck, 2017). The daily GNSS solutions refer to the IGS14 realization of the ITRF2014 (Altamimi *et al*., 2016).

For the episodic surveys, GNSS data have been processed for the entire observation period of each survey, whereas data from permanent GNSS sites were analysed in continuous 168-hour sessions. In both cases, the data sampling interval was 30 seconds.

The analysed GNSS data set comprises a set of 3D (North, East, Up) site positions for each episodic survey, with which the velocities are determined through the respective difference between surveys. For the permanent GNSS sites, we used time series of the weekly solutions with the 3D positions. In this case, the velocities were computed through a least squares procedure to remove annual and semi-annual periodicities.

IV. 2D STRAIN CALCULATION

We used the horizontal velocities to compute the bi-dimensional (2D) infinitesimal strain from various sets of 3 non-co-linear GNSS stations each, forming triangles, as formulated by Jaeger *et al*. (2007) for a flat Earth. Thus, if u_x , u_y denote the components of the displacement vector, the partial derivatives along the *x* and *y* directions, at point (*x, y*), represent the respective normal strains, ε_{xx}, ε_{yy}, that is (Eq. 1):

$$\varepsilon_{xx} = \frac{\partial u_x}{\partial x}, \varepsilon_{yy} = \frac{\partial u_y}{\partial y} \quad (1)$$

The other two components of the strain matrix are considered symmetrical, $\varepsilon_{xy} = \varepsilon_{yx}$. By setting *i = 1, 2,* ε_1 and ε_2 define the two principal horizontal strains, which can be computed as (Eq. 2):

$$\varepsilon_i = \varepsilon_{yy} cos^2\theta_i + \varepsilon_{xx} sin^2\theta_i + \varepsilon_{xy} sin\theta_i cos\theta_i \quad (2)$$

where θ_i = principal directions, i=*1*, *2*

In our analysis, we have determined the elongation/shortening (i.e., the ratio u/l in strain units, 10^{-9}; l being the undeformed baseline length) the dilatation and the principal strains for triplets of GNSS sites according to the respective differences between surveys.

Figure 2 shows the distribution of areal strain along the island with significant changes when we compare each GNSS survey with the first one carried on in 2015. The west sector of the island displays a compression pattern, which increases in magnitude as successive campaigns advance along the years. Some smaller compressive sectors come out in the central and north-eastern areas of the island during 2017 and 2018. The central and east sectors of the island evidence a dilatation pattern, which slightly varies its magnitude along the years. If we consider the maximum lapse between surveys (4.7 years) for the period 2019-2015(1), the strain pattern still remarks the two compressive-extensional regimes, the highest strain values corresponding to a dilatation regime located in the centre-east of the island.

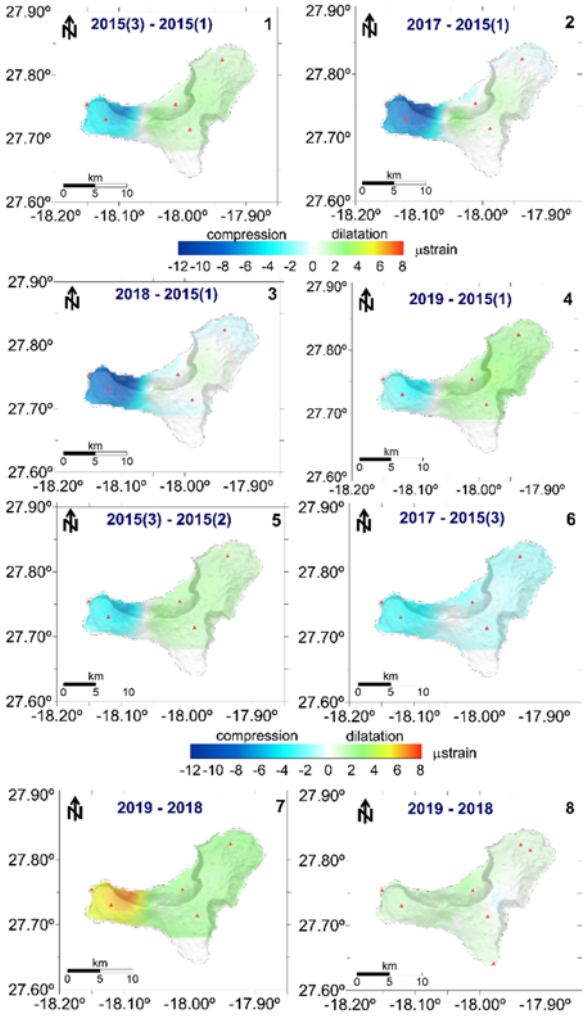

Figure 2. Contour maps of the areal strain computed as for the difference with the first survey (panels 1 to 4) and for the difference survey by survey (panels 5 to 7). The panel 8 includes the permanent GNSS sites LRES and EH01 in the calculation. Red triangles show the location of the GNSS sites.

Similarly, we have computed the areal strain based on the difference between subsequent surveys (Figure 2). The strain pattern exhibits changes in the magnitude that are not observed when the first survey is fixed as a reference. Thus, the dilatation pattern in the central and east sectors of the island vanishes during year 2017, and it moves to west and central areas during year 2018. Furthermore, the year 2018 shows a significant difference in the strain with regard to 2019 as the dilatation pattern is completely extended along the island, with the maximum values located in the westernmost area of the island.

In addition, we have calculated the 2D maximum shear strain through the angle between the positions before and after the deformation. That is (Eq. 3),

$$\varepsilon_{xy} = \frac{1}{2}\left(\frac{\partial u_x}{\partial x} + \frac{\partial u_y}{\partial y}\right) \qquad (3)$$

Which in terms of the principal horizontal strains (2) is computed as $\frac{1}{2}(\varepsilon_1 - \varepsilon_2)$. Figure 3 shows the results for the maximum shear strain thus calculated, which are in accordance with the surface distribution of the areal strain. This is clearly seen through the comparison of each survey with the first one of 2015. Most of the NW rift sector shows the highest shear strain values found along the island, which increase in magnitude by the middle of 2017 and subsequently towards the end of 2018.

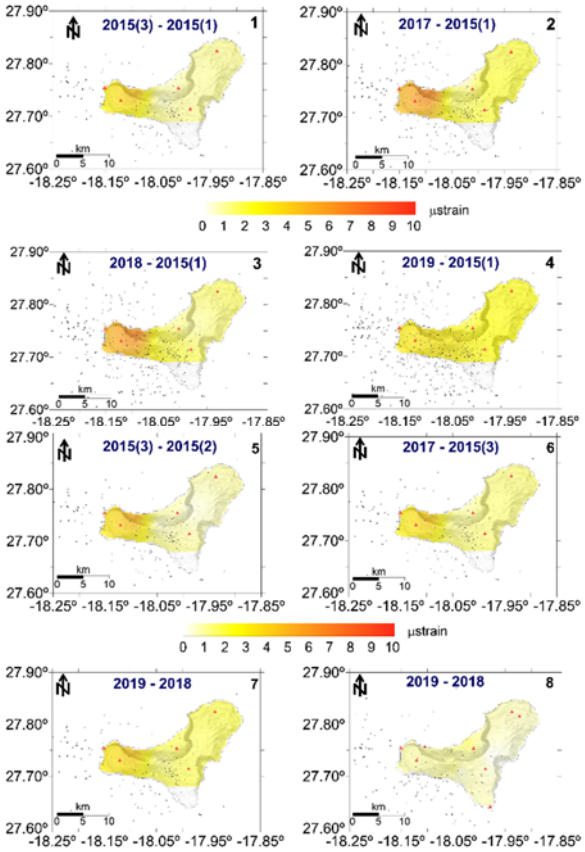

Figure 3. Same contour map as Figure 2 but for the maximum shear strain. The grey circles are the epicentres of the earthquakes (m_{bLG} 1.2 to 3.9) recorded during the respective time intervals.

By including the stations LRES and EH01 for the time difference 2019-2018 (panel 8 in Figures 2 and 3), then the areal strain and the maximum shear strain evidence a lower magnitude, and specific areas located to the North and in the NW rift of the island show the greatest values. This is a consequence of the larger surface area involved in the calculation, which consequently causes the strain and maximum shear strain to be stretched.

Because there are no more than 3 permanent stations with publicly accessible data (FRON, LRES, EH01), we have installed the GNSS site named BALN at the north of the island (see Figure 1). Consequently, it is possible to form a radial GNSS geodetic network configuration to deepen into this ground deformation study. Actually, we can define three quasi-equilateral triangles covering the three-armed rift structure of the island, which favours the condition of homogeneity that is required for reliable 2D strain results (Figure 4). Such network configuration makes it possible to study the

concordance with the results from the GNSS episodic surveys, and to check for alterations in the deformation pattern to a larger scale. The results from the strain and maximum shear strain calculation encompassing 2019-2021 time interval are shown in Figure 4.

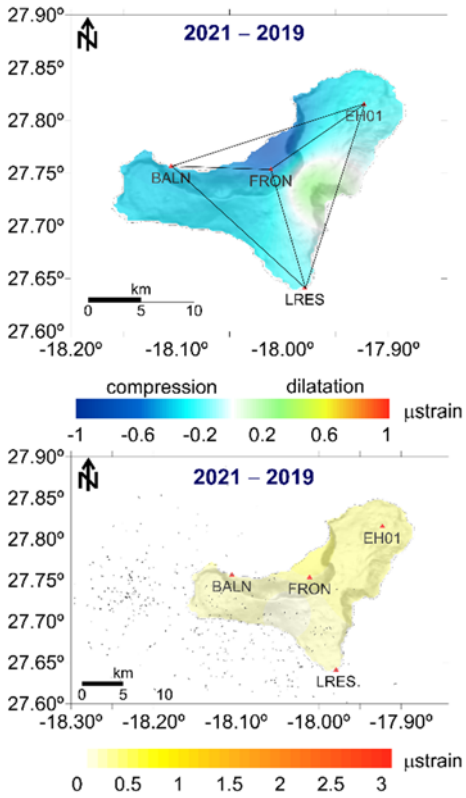

Figure 4. (Up) Areal strain computed for the difference 2021-2019 using the permanent GNSS sites LRES, EH0, FRON and the most recent site BALN. The quasi-equilateral triangles used for the segmentation approach are also indicated. (Down) Maximum shear strain computed as for the difference 2021-2019. The dots are the epicentres of the earthquakes (m_{bLG} 1.2 to 3.9) recorded during the indicated time interval.

V. Discussion of results

During the period 2015 to 2019 that follows the post-eruptive episodes identified between 2012 and 2014 (*e.g.*, Klügel *et al.*, 2015), the seismic activity became less intense in El Hierro. About 500 earthquakes from low to moderate magnitude (m_{bLG} 2 to m_{bLG} 3.9) were recorded in the seismic catalogue of the Spanish IGN (www.ign.es). According to our analysis of the episodic GNSS observations, the ground displacement measured is of lower magnitude, still remaining an uplift trend (from 1 to 6.5 cm) in the central and NE sector of the island and a slight subsidence (about 0.8 cm) in the W sector up to 2017. This behaviour is followed by stability in the central zone of El Hierro and a subsidence of about 3.0 cm in the NE and W rifts until the end of 2019. In addition, the time series analysis of the four continuous GNSS sites (BALN, FRON, EH01, LRES) report an average ground subsidence of about 8 mm from 2019 to 2021.

The Figure 5 summarizes the time variation of the length of the baselines computed with respect to the first survey 2015(1). As we are using data from repeated surveys (2015 to 2019), it is reasonable to assume 1 cm change in the baseline length as a limit of detectability of deformations.

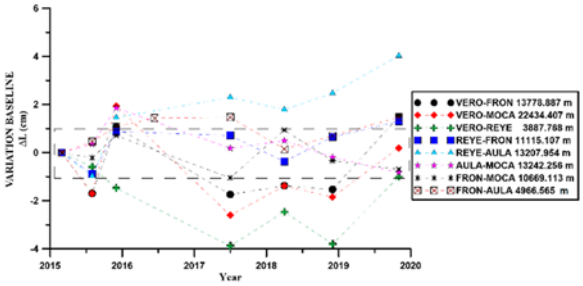

Figure 5. Time change of the baseline's length calculated for the GNSS episodic surveys carried out for the period 2015-2019. The gray rectangle visually provides an order of magnitude for the reliability of the length changes assessed from the repeated surveys.

Stations VERO and REYE (Figure 5), in the West sector, display the largest dynamics among the considered stations. The shortening in VERO-REYE might confirm that the west sector of El Hierro undergoes a compression. This is a quite obvious derivation, because the strain comes from the displacements assessed among pair of stations (baselines), namely the sides of the triangles. Otherwise, the baseline REYE-AULA (Figure 5) would confirm a dilatation in the central sector.

The strain pattern calculated through episodic GNSS points out two compressive-extensional regimes in El Hierro (Figure 2). The maximum shear strain results are in accordance with the surface distribution of the areal strain, and the NW rift of the island exhibits the highest values while the seismicity is mostly concentrated in the central and West sectors of the island (Figure 3). That fact could be a consequence of the magma accumulation and/or displacement in depth during the period of time analysed here. Indeed, seismicity recorded during this period (Figure 6) is spatially extensive and it is mostly located at 10-15 km in depth, which corresponds to the lower oceanic crust area, and 15-25 km, which corresponds to areas of different magma reservoirs during the eruption phase and other level of emplacement of sill-like magma intrusions during the post-eruptive phase (Longpré *et al.*, 2014; Klügel *et al.*, 2015). The seismicity for the period 2019-2021 is more homogeneously distributed for the depths 10-22 km and 30-40 km.

The unrest episode that preceded the last eruption in El Hierro involved a winding dyke propagation as local crustal structures and discontinuities diverted the magma pathway (*e.g.*, Martí *et al.*, 2013; Gorbatikov *et al.*, 2013; Sainz-Maza *et al.*, 2014). A similar situation was produced during the 2012-2014 post-eruptive stage, which involved six different magmatic intrusions, as suggested by the seismicity and the ground

deformation produced as a consequence of the lateral magma movement in depth across the island's edifice (Klügel *et al*., 2015; Domínguez-Cerdeña *et al*., 2018). However, this has not been the case since 2015 in advance, although the strain patterns obtained in this study suggest a kind of dipole behaviour in terms of stress change for the period studied here. Such dipole structure evidences slight time changes, as suggested through the strain differences computed survey by survey (Figure 2). That is, the difference between subsequent surveys exhibits changes in the strain magnitude that are not observed when the first survey is fixed as a reference. For instance, the dilatation pattern in the central and east sectors of the island vanishes during year 2017, and it moves to west and central areas during year 2018. In addition, the year 2018 shows a significant difference in the strain with regard to 2019 as the dilatation pattern is completely extended along the island, with the maximum values located in the westernmost area of the island. The period of time analysed here points out the stress distribution inside the crust and possibly reveals the tectonic stresses across the island's edifice, as a consequence of the previous eruption and post-eruptive activity.

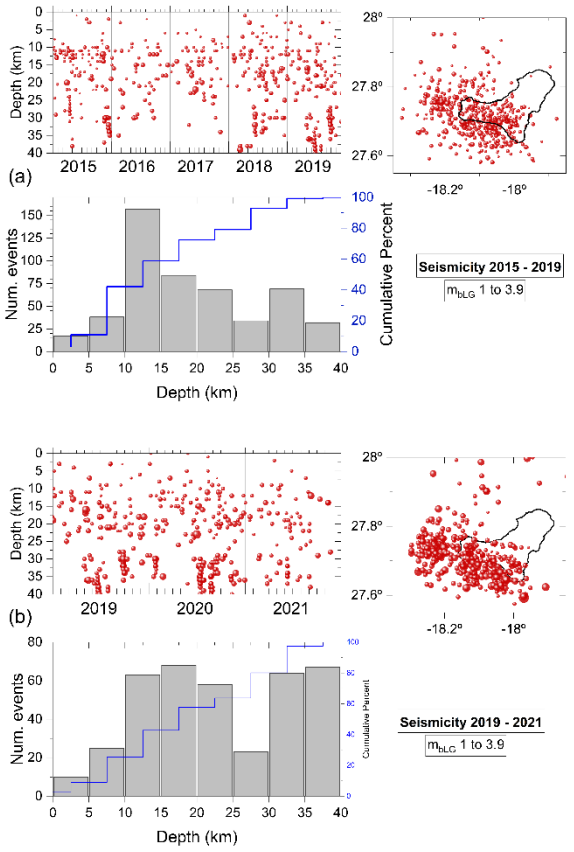

Figure 6. (a) Seismicity recorded at El Hierro Island from 2015 to 2019. Panels show the location, distribution in depth and a bar diagram with the cumulative number of earthquakes. (b) Same as (a) but for the period 2019 to 2021.

VI. Conclusions

Based on the analysis of continuous and survey GNSS data spanning 2015-2019 time interval, we have tried to image the deformation pattern in El Hierro Island. The strain pattern retrieved from episodic GNSS surveys displays a peculiar pattern depending on how data are taken into account. A kind of dipole strain field, slightly changing over time, emerges when strain is computed from the difference between subsequent surveys, with two compressive-extensional regimes in the west and central-east sectors of the island respectively. Such a dipole structure becomes less evident when the first survey is fixed as a reference. However, considering that the dipolar field emerges from the deformation obtained from the most temporally spaced pair of surveys (2019-2015), when most of the deformation has been accumulated, we believe that in the time interval covered by the present study this is the deformation field that characterises El Hierro. The maximum shear strain field appears to be in accordance with the surface distribution of the areal strain, and the NW rift of the island exhibits the highest values, while the seismicity is mostly concentrated in the central and West sectors of the island. In fact, the crustal heterogeneity and the six post-eruptive intrusions associated with intense seismic swarms and inflation, which did not produce an eruption, but lateral magma movements could have affected the observed strain field. The reconstructed strain field could be compatible with a magma accumulation and/or displacement. The results of our study allowed us to highlight the distribution of deformation in response to tectonic stresses within the crust and the island`s edifice, as a consequence of previous eruption and post-eruptive activity.

VII. Acknowledgements

Projects PID2019-104726GB-I00 and CGL2015-63799-P of the Spanish Research Agency has supported this research. We wish to acknowledge GRAFCAN (www.grafcan.es) of the Government of the Canary Islands for providing GNSS data from permanent station FRON. Likewise, to the Spanish IGN (www.ign.es) for providing the EH01 and LRES data.

References

Altamimi, Z., Rebischung, P., Métivier, L., and Collilieux, X. (2016). ITRF2014: A new release of the International Terrestrial Reference Frame modeling nonlinear station motions. *Journal of Geophysical Research,* Vol., 121, pp. 6109–6131.

Arnoso, J., U. Riccardi, M. Benavent, U. Tammaro, FG. Montesinos, I. Blanco-Montenegro, and E. Vélez (2020). Strain pattern and kinematics of the Canary Islands from GNSS time series analysis. *Remote Sensing*, Vol. *12*, 3297, DOI: 10.3390/rs12203297.

Banville, S. (2020). CSRS-PPP Version 3: Tutorial, p. 11. https://webapp.geod.nrcan.gc.ca/geod/tools-

outils/sample_doc_filesV3/NRCan%20CSRS-PPP-v3_Tutorial%20EN.pdf.

Berrocoso, M., Carmona, J., Fernandez-Ros, A., Pérez-Pena, A., Ortiz, R., and García, A. (2010). Kinematic model for Tenerife Island (Canary Islands, Spain): Geodynamic interpretation in the Nubian plate context. *Journal of African Earth Sciences,* Vol. 58, pp. 721–733, DOI: 10.1016/j.jafrearsci.2010.04.007.

Cantagrel, J.M., Arnaud, N.O., Ancochea, E., Fuster, J.M., and Huertas, M.J., (1999). Repeated debris avalanches on Tenerife and genesis of Las Cañadas caldera wall (Canary Islands). *Geology* 27, pp. 739– 742.

Carracedo, J. C., E. R. Badiola, H. Guillou, J. de la Nuez, and F. J. Perez-Torrado (2001). Geology and volcanology of La Palma and El Hierro, Western Canaries. *Estudios Geológicos*, Vol. 57, pp. 175–273.

Domínguez-Cerdeña, I., L. García-Cañada, M.A. Benito-Saz, C. del Fresno, H. Lamolda, J. Pereda de Pablo, and C. Sánchez Sanz, (2018). On the relation between ground surface deformation and seismicity during the 2012–2014 successive magmatic intrusions at El Hierro Island. *Tectonophysics*, Vol. 744, pp. 422-437, DOI: 10.1016/j.tecto.2018.07.019.

García, A., Fernández-Ros, A., Berrocoso, M., Marrero, J.M., Prates, G., De La Cruz-Reyna, S., and Ortiz, R. (2014). Magma displacements under insular volcanic fields, applications to eruption forecasting: El Hierro, Canary Islands, 2011–2013. *Geophysical Journal International*, Vol. 197, pp. 322–334.

Geyer, A., Marti, J., and Villaseñor, A. (2016). First-order estimate of the Canary Islands plate-scale stress field: Implications for volcanic hazard assessment. *Tectonophysics*, Vol. 679, pp. 125–139.

Gorbatikov, A.V., Montesinos, F.G., Arnoso, J., Benavent, M., and Tsukanov, A.A. (2013). New features in the subsurface structure model of El Hierro Island (Canaries) from low-frequency microseismic sounding: an insight into the 2011 seismo-volcanic crisis. Surveys in Geophysics, Vol. 34, pp. 463–489. DOI: 10.1007/s10712-013-9240-4.

Jaeger, J.C., Cook, N.G.W., and Zimmerman, R.W. (2007). Fundamentals of Rock Mechanics, 4th ed. Blackwell Publishing Ltd. USA, ISBN 13: 978-0-632-05759-7.

Klügel, A., MA. Longpré, L. García-Cañada, and J. Stix (2015). Deep intrusions, lateral magma transport and related uplift at ocean island volcanoes. *Earth and Planetary Science Letters*, Vol. 431, pp. 140-149. DOI: 10.1016/j.epsl.2015.09.031.

Longpré, M.A., A. Klügel, A. Diehl, and J. Stix (2014). Mixing in mantle magma reservoirs prior to and during the 2011–2012 eruption at El Hierro, Canary Islands. *Geology*, Vol. 42, pp. 315–318. DOI: 10.1130/g35165.1.

López, C., García-Cañada, L., Martí, J., and Cerdeña, I.D. (2017). Early signs of geodynamic activity before the 2011–2012 El Hierro eruption. *Journal of Geodynamics,* Vol. 104, pp. 1–14.

Martí, J., V. Pinel, C. López, A. Geyer, R. Abella, M. Tárraga, M. J. Blanco, A. Castro, and C. Rodriguez (2013). Causes and mechanisms of El Hierro submarine eruption (2011–2012) (Canary Islands). *Journal of Geophysical Research, Solid Earth*, Vol. 118, pp. 823–839, DOI: 10.1002/jgrb.5008.

Pérez-Plaza, S., Berrocoso, M., Rosado, B., Prates, G., and Fernández-Palacín, F. (2021). The time lag between deformation process and seismic activity in El Hierro Island during the eruptive process (2011–2014): a functional phased approach. *Earth, Planets and Space*, Vol. 73, No. 1. DOI: 10.1186/s40623-021-01514-0.

Ray, R.D. (1999). A global ocean tide model from Topex/Poseidon altimetry: GOT99.2, NASA Tech. Memo., 209478

Ray, R.D. (2013). Precise comparisons of bottom-pressure and altimetric ocean tides. *Journal of Geophysical Research, Oceans*, Vol. 118, pp. 4570–4584. DOI:10.1002/jgrc.20336

Riccardi, U., Arnoso, J., Benavent, M., Vélez, E., Tammaro, U., and Montesinos, F.G. (2018). Exploring deformation scenarios in Timanfaya volcanic area (Lanzarote, Canary Islands) from GNSS and ground based geodetic observations. *Journal of Volcanology and Geothermal Research*, 357, pp. 14-24. DOI: 10.1016/j.volgeores.2018.04.009

Sainz-Maza Aparicio, S., Arnoso Sampedro, J., Montesinos, F. G., and Marti Molist, J. (2014) *Volcanic signatures in time gravity variations during the volcanic unrest on El Hierro (Canary Islands).* *Journal of Geophysical Research - Part B - Solid Earth*, 119 (6). pp. 5033-5051.

Tammaro, U., DeMartino, P., Obrizzo, F., Brandi, G., D'Alessandro, A., Dolce, M. Malaspina, S., Serio, C., and Pingue, F. (2013). Somma Vesuvius volcano: Ground deformations from CGPS observations (2001–2012). *Annals of Geophysics*, Vol. 56, No. 4, S0456, DOI: 10.4401/ag-6462.

Teunissen, P.J.G., and Montenbruck, O. (2017). Springer Handbook of Global Navigation Satellite Systems. Springer International Publishing, Cham. DOI: 10.1007/978-3-319-42928-1.

Segall P. (2010). Earthquake and volcano deformation. Princeton University Press, pp. 432.

Wu, Y., Jiang, Z.-S., Yang, G., Wei,W., and Liu, X. (2011). Comparison of GPS strain rate computing methods and their reliability. *Geophysical Journal International*, Vol. 185, pp. 703–717. DOI: 10.1111/j.1365-246X.2011.04976.x